

Superconductivity in Weyl Semimetal Candidate MoTe₂

Yanpeng Qi¹, Pavel G. Naumov¹, Mazhar N. Ali², Catherine R. Rajamathi¹, Walter Schnelle¹, Oleg Barkalov¹, Michael Hanfland³, Shu-Chun Wu¹, Chandra Shekhar¹, Yan Sun¹, Vicky Süß¹, Marcus Schmidt¹, Ulrich Schwarz¹, Eckhard Pippel⁴, Peter Werner⁴, Reinald Hillebrand⁴, Tobias Förster⁵, Erik Kampert⁵, Stuart Parkin⁴, R. J. Cava², Claudia Felser¹, Binghai Yan^{1,6*}, Sergey A. Medvedev^{1*}

¹Max Planck Institute for Chemical Physics of Solids, 01187 Dresden, Germany

²Department of Chemistry, Princeton University, Princeton, New Jersey 08544, USA

³European Synchrotron Radiation Facility, BP 220, Grenoble 38043, France

⁴Max Planck Institute of Microstructure Physics, 06120 Halle, Germany

⁵Dresden High Magnetic Field Laboratory (HLD-EMFL), Helmholtz-Zentrum Dresden-Rossendorf, 01328 Dresden, Germany

⁶Max Planck Institute for the Physics of Complex Systems, 01187 Dresden, Germany

* E-mail: Yan@cpfs.mpg.de, Sergiy.Medvediev@cpfs.mpg.de

Abstract

Transition metal dichalcogenides have attracted research interest over the last few decades due to their interesting structural chemistry, unusual electronic properties, rich intercalation chemistry and wide spectrum of potential applications. Despite the fact that the majority of related research focuses on semiconducting transition-metal dichalcogenides e.g., MoS₂, recently discovered unexpected properties of WTe₂ are provoking strong interest in semimetallic transition metal dichalcogenides featuring large magnetoresistance, pressure-driven superconductivity, and Weyl semimetal state. We investigate the sister compound of WTe₂, MoTe₂, predicted to be a Weyl semimetal and a quantum spin Hall insulator in bulk and monolayer form, respectively. We find that bulk MoTe₂ exhibits superconductivity with a transition temperature of 0.10 K and application of external pressure dramatically enhances the transition temperature up to maximum value of 8.2 K at 11.7 GPa. Observed dome-shaped superconductivity phase diagram provides insights into the interplay between superconductivity and topological physics.

Transition-metal dichalcogenides (TMDs) have attracted tremendous attention due to their rich physics and promising potential applications¹⁻¹¹. TMDs share the same formula, MX_2 , where M is a transition metal (e.g., Mo or W) and X is a chalcogenide atom (S, Se, and Te). These compounds typically crystallize in many structures, including 2H-, 1T-, 1T'-, and T_d -type lattices. The most common structure is the 2H phase, where M atoms are trigonal-prismatically coordinated by the chalcogenide atoms. These planes then stack upon one other with van der Waals gaps inbetween. In contrast, the 1T structure corresponds to octahedral coordination of M. The 1T' phase is a monoclinic lattice that can be interpreted as a distortion of the 1T phase by the formation of in-plane M-M bonds, resulting in a pseudo-hexagonal layer with zigzag metal chains. Finally, the T_d phase is very similar to the 1T' phase, but the layers stack in a direct fashion, resulting in a higher-symmetry orthorhombic structure. Depending on the synthesis technique, the same composition of MX_2 can crystallize in a variety of structures with very different electronic properties. For example, MoTe_2 exists in 2H, 1T', and T_d structures^{12,14}, while WTe_2 has commonly been observed in the T_d structure¹⁵. The 2H and 1T compounds are primarily semiconducting, whereas the 1T' and T_d compounds are typically semimetallic.

Very recently, semimetallic TMDs have attracted considerable attention because of the discovery of salient quantum phenomena. For instance, T_d-WTe₂ has been found to exhibit an extremely large magnetoresistance^{16,17}, pressure (P)-driven superconductivity (highest resistive transition temperature $T_c \approx 7$ K at 16.8 GPa)^{18,19}, and a large and linear Nernst effect²⁰. Further, this material has been theorized to constitute the first example of a type-II Weyl semimetal²¹. Moreover, the 1T'-MX₂ monolayer has been predicted to be a 2D topological insulator⁶.

The discovery of superconductivity in WTe₂ is apparently contradictory to previous theoretical predictions²², which claim that 2H TMDs may become superconducting at high P , but the 1T' phases will not. Thus the investigation of other TMDs for the appearance of superconductivity under pressure is of big interest. Molybdenum ditelluride (MoTe₂) is unique among the TMDs since it is the only material that can be grown in both 2H and 1T' forms, allowing for direct examination of this theory. If superconductivity exists in 1T'-MoTe₂, it may allow the topological edge states to also become superconducting, because of the proximity effect in a bulk superconductor. This would open up a new platform for the study of topological superconductivity, which has potential application in quantum computation²³. Regarding the recently anticipated Weyl semimetal (WSM) phase in MoTe₂ (Ref. 24),

discovery of superconductivity may introduce a new pathway for the exploration of topological superconductivity^{25,27} along with emergent space-time supersymmetry²⁸.

Here, we report on the transport properties of the 2H, 1T', and T_d polytypes of MoTe₂ under various applied P . We find that T_d-MoTe₂ exhibits superconductivity with $T_c = 0.10$ K, according to electrical resistivity (ρ) measurements. Application of relatively low pressures below 1 GPa dramatically enhances the T_c , and a dome-shaped T_c - P phase diagram is observed with maximum $T_c = 8.2$ K at 11.7 GPa; this is approximately 80 times larger than the ambient pressure value. In contrast, we do not observe any traces of superconductivity in the 2H phase, even when it becomes metallic under P . We assume that the extreme sensitivity of the superconductivity to P is a consequence of the unique electronic structure. Thus, MoTe₂ presents the opportunity to study the interaction of topological physics and superconductivity in a bulk material.

Results

Structure and transport properties at ambient pressure

Prior physical properties measurements, synthesized 1T'-MoTe₂ samples were characterized using single-crystal x-ray diffraction (SXRD) and high-angle annular dark-field scanning transmission electron microscopy (HAADF-STEM). The atomic

arrangement of the 1T' structure was determined using high-resolution HAADF-STEM images and diffraction patterns, as shown in Fig. 1a, b and Supplementary Fig. 1a, b. The crystal structures of 1T' and T_d-MoTe₂ are sketched in Fig. 1c. At room temperature, the crystals exhibit the expected monoclinic 1T'-MoTe₂ structure, while the SXRD measurements at 120 K indicate a transition into the orthorhombic T_d structure. 1T'-MoTe₂ structure crystallizes in the $P2_1/m$ space group with lattice parameters of $a = 6.320 \text{ \AA}$, $b = 3.469 \text{ \AA}$, $c = 13.86 \text{ \AA}$, and $\beta = 93.917^\circ$; these results are consistent with the previously reported structure¹². The Raman spectra at ambient P contain two characteristic peaks (Supplementary Fig. 1c), which are due to the A_g and B_g vibrational modes of the 1T'-MoTe₂ structure; this is also in agreement with a previous report²⁹. A full structural solution was obtained for the orthorhombic T_d phase at 120 K, the refined parameters are given in Supplementary Tables 1 and 2.

Temperature dependence of electrical resistivity of MoTe₂ down to a minimum temperature of $T_{\min} = 0.08 \text{ K}$ at ambient pressure is presented in Fig. 2. In contrast to the 2H phase, which displays semiconducting behavior, 1T'-MoTe₂ is semimetallic in nature. At zero field, the room-temperature resistivity is $\rho = 1.0 \times 10^{-5} \Omega \text{ m}$, which decreases to $2.8 \times 10^{-7} \Omega \text{ m}$ at 0.5 K, yielding a residual resistance ratio (RRR) ≈ 36 . At $T \approx 250 \text{ K}$ an anomaly with thermal hysteresis (Fig. 2a, inset) is observed, which is

associated with the first-order structural phase transition from the 1T' to the T_d polytype^{14,30}. A range of magneto-transport properties has been measured at zero pressure on our MoTe₂ crystals (Supplementary Figs. 2-4 and Supplementary Note 1). From Hall effect measurements, MoTe₂ shows dominant electron-type transport. Within a single-band model the electron concentration n_e is estimated to $5 \times 10^{19} \text{ cm}^{-3}$ at 2 K and $8 \times 10^{20} \text{ cm}^{-3}$ at 300 K (Supplementary Fig. 2), which is close to reported value²⁹. In addition, T_d-MoTe₂ gradually becomes superconducting below $T \sim 0.3 \text{ K}$ (the onset of transition), while zero resistance is observed at $T_c = 0.10 \text{ K}$ (Fig. 2b). Note that, although potential superconductivity at $\sim 0.3 \text{ K}$ in MoTe₂ has been briefly mentioned in the literature³¹, no related data have been published.

1T' – T_d structural transition under pressure

It is well known that high pressure can effectively modify lattice structures and the corresponding electronic states in a systematic fashion. Hence, we measured $\rho(T)$ for the same 1T'-MoTe₂ single crystal at various pressure values P (Fig. 3). Fig. 3a shows the typical $\rho(T)$ curves for P up to 34.9 GPa. For increasing P , the metallic characteristic increases and ρ decreases over the entire temperature range. At low pressures, resistance curves exhibit an anomaly at a temperature T_s , associated with the monoclinic 1T' – orthorhombic T_d structural phase transition similarly to the ambient pressure data. With

pressure increase, the resistivity anomaly becomes less pronounced whereas the temperature of anomaly T_s is significantly shifted to lower T and disappears completely above 4 GPa. Thus, the application of P tends to stabilize the monoclinic phase. In addition, the Raman spectra recorded at room temperature under different pressures (Fig. 4a) contain only two characteristic peaks for the $1T'$ -structure A_g and B_g modes²⁹. The frequencies of both vibrational modes increase gradually with no discontinuities as P increases (Fig. 4b) indicating the absence of major structural phase transition in the whole studied pressure range at room temperature. SXRD data (Fig. 4c and Supplementary Fig. 5) also indicate that application of pressure stabilizes the monoclinic $1T'$ structure. Increase of P at room temperature results in enhancement of monoclinic distortion (increase of the monoclinic angle β). In an isothermal run at 135 K the reversible orthorhombic T_d to monoclinic $1T'$ transition is observed at ≈ 0.8 GPa (≈ 0.4 GPa) at pressure increase (decrease) (Fig. 4c). Thus, application of P well below 1 GPa decreases the temperature of structural transition to below 135 K. Furthermore, at $P \approx 1.5$ GPa, the $1T'$ structure remains stable down to at least 80 K. The quantitative discrepancy in the T_s values derived from structural and resistivity data is most likely due to nonhydrostatic pressure conditions in the resistivity measurements, and the thermal hysteresis since the resistivity curves are recorded with increasing temperatures.

The stability of MoTe₂ in different phases can be explained using total energy calculations within density-functional theory (DFT). The optimized lattice constants are very close to experimental values for both two phases, as shown in Supplementary Fig. 6 and Supplementary Table 3. After evaluating the total energies of the two phases at ambient pressure, we found that the T_d phase exhibits slightly lower energy (0.5 meV per formula unit) than the 1T' phase. This is consistent with the fact that the low- and high-*T* phases are T_d and 1T', respectively, without external pressure. As the 1T' phase can be obtained by sliding between layers of the T_d phase, the former exhibits a slightly smaller equilibrium volume than the latter, as also revealed from the lattice parameters measured via SXRD. As illustrated by the energy-volume profile in Fig. 1d, external pressure will stabilize the 1T' phase with the smaller volume (and correspondingly higher density) by increasing the shift between neighboring layers.

The dome-shaped superconductivity behavior

Our pressure studies have revealed that the T_c is very sensitive to pressure. That is, T_c increases dramatically to 5 K at relatively low pressures below 1 GPa, before beginning a slower increase to a maximum T_c of 8.2 K at 11.7 GPa (Figs. 3b, 5). Beyond this pressure, T_c decreases and no superconductivity with $T_c > 1.5$ K is found at $P > 34.9$ GPa (Fig. 3c). Remarkably, the drastic increase of T_c at low pressures is associated with

sharp decrease of temperature of 1T' - T_d structural phase transition T_s . Subsequently at higher pressures, T_c still increases to its maximum value with increasing P but with significantly lower rate. Our findings demonstrate that the strong enhancement of T_c under high P is associated with suppression of the 1T' - T_d structural phase transition. All the characteristic temperatures in the above experimental results are summarized in the T - P phase diagram in Fig. 5. A dome-shaped superconducting phase boundary is obtained for MoTe₂, with a sharp slope towards the zero- P end of the diagram.

The bulk character of the superconductivity is confirmed by observations of the magnetic shielding effect in the low pressure range and at 7.5 GPa (Supplementary Fig. 7). The onset temperatures of the diamagnetism are consistent with that of the resistivity drop and confirm the drastic increase of T_c in the low pressure range (Fig. 5). Further, we conducted resistivity measurements in the vicinity of T_c for various external magnetic fields. As can be seen in Fig. 3d, the zero-resistance-point T_c under $P = 11.2$ GPa is gradually suppressed with increasing field. Deviating from the Werthamer-Helfand-Hohenberg theory based on the single-band model, the upper critical field, $H_{c2}(T)$, of MoTe₂ has a positive curvature close to T_c ($H = 0$), as shown in Fig. 3e. This is similar to the behaviors of both WTe₂ (Ref. 18) and NbSe₂ (Ref. 32). The experimental $H_{c2}(T)$ data can be described within the entire T/T_c range by the

expression $H_{c2}(T) = H_{c2}^* (1 - T/T_c)^{1+\alpha}$ (Refs. 18, 33). The fitting parameter $H_{c2}^* = 4.0$ T can be considered as the upper limit for the upper critical field $H_{c2}(0)$, which yields a Ginzburg–Landau coherence length $\xi_{GL}(0)$ of ~ 9 nm. The corresponding data obtained at $P = 1.1$ GPa is also shown in Fig. 3e. It is also worth noting that our estimated value of $H_{c2}(0)$ is well below the Pauli-Clogston limit.

We repeated the high-pressure experiments using different crystal flakes. Similar superconducting behavior with almost identical T_c was observed. For comparison with 1T'-MoTe₂, we also measured $\rho(T)$ for the 2H-MoTe₂ single crystal at various pressure values. We found a pressure-induced metallization at 15 GPa (Supplementary Fig. 8), which is consistent with previous theoretical predictions²². However, in contrast, we did not detect any signature of superconductivity in the 2H phase for pressures up to 40 GPa.

Discussion

For MoTe₂, the superconducting behavior in the low- P region clearly differs from that in the high- P region. Under quite low P , the sharp increase in T_c is concomitant with a strong suppression of the structural transition, which is reminiscent of observations for other superconductors with various kinds of competing phase transitions. The drastic increase of the T_c occurs within the T_d phase, which is shown by

DFT calculations to be a Weyl semimetal (Supplementary Fig. 9a and Supplementary Note 2) with a band structure around the Fermi level which is extremely sensitive to changes in the lattice constants^{24, 34}. Thus, one can expect that dramatic structural and electronic instabilities emerge in the low- P region, which may account for the strong enhancement of T_c . At higher pressures, the topologically trivial (due to inversion and time reversal symmetry) 1T' phase (Supplementary Fig. 9b and Supplementary Note 2) remains stable in the whole temperature range. Although within this phase T_c still continues to increase up to its maximum value, the rate of the increase is significantly lower and this growth is naturally explained by the increase of the electronic density of states at the Fermi level in the 1T' phase (Supplementary Fig. 9c). Thorough exploration of superconductivity in MoTe₂ from both experimental and theoretical perspectives is required.

Methods

Single-crystal growth

1T'-MoTe₂ crystals were grown via chemical vapor transport using polycrystalline MoTe₂ powder and TeCl₄ as a transport additive³⁵. Molar quantities of Mo (Sigma Aldrich 99.99%) were ground in combination with purified Te pieces (Alfa Aesar

99.99%), pressed into pellets, and heated in an evacuated quartz tube at 800 °C for 7 days. Crystals were obtained by sealing 1 g of this powder and TeCl₄ (3 mg/ml) in a quartz ampoule, which was then flushed with Ar, evacuated, sealed, and heated in a two-zone furnace. Crystallization was conducted from (T_2) 1000 to (T_1) 900 °C. The quartz ampoule was then quenched in ice water to yield the high-temperature monoclinic phase. The obtained crystals were silver-gray and rectangular in shape. 2H-MoTe₂ crystals were grown using a similar method, but without quenching.

Structural and transport measurements at ambient pressure

The structures of the MoTe₂ crystals were investigated using single-crystal x-ray diffraction (SXRD) with Mo K_α radiation. In order to analyze the atomic structure of the material, high-angle annular dark-field scanning transmission electron microscopy (HAADF-STEM) was performed. The dependence of the electrical resistivity ρ on temperature T was measured using a conventional four-probe method (low-frequency alternating current, PPMS, Quantum Design). Temperatures down to 0.08 K were achieved using a home-built adiabatic demagnetization stage. The pulsed magnetic field experiments were conducted at the Dresden High Magnetic Field Laboratory (Helmholtz-Zentrum Dresden-Rossendorf, HLD-HZDR).

Experimental details of high pressure measurements

A non-magnetic diamond anvil cell was used for ρ measurements under P values of up to 40 GPa. A cubic BN/epoxy mixture was used for the insulating gaskets and Pt foil was employed in the electrical leads. The diameters of the flat working surface of the diamond anvil and the sample chamber were 500 and 200 μm , respectively. The initial sample thickness was $\approx 40 \mu\text{m}$. The value of ρ was measured using the dc current in van der Pauw technique in a customary cryogenic setup (lowest achievable temperature 1.5 K) at zero magnetic field, and the magnetic field measurements were performed on a PPMS. Pressure was measured using the ruby scale³⁶ by measuring the luminescence from small chips of ruby placed in contact with the sample.

Magnetization was measured on MoTe_2 ($m = 3.1 \text{ mg}$) in a pressure cell ($m = 170 \text{ mg}$) for $P \leq 0.7 \text{ GPa}$ and $T \geq 0.5 \text{ K}$ (Quantum Design MPMS, iQuantum ^3He insert). Shielding (after zero-field cooling) and Meißner effect curves (in field-cooling) were recorded.

The high- P Raman spectra were recorded using a customary micro-Raman spectrometer with a HeNe laser as the excitation source and a single-grating spectrograph with 1 cm^{-1} resolution. Raman scattering was calibrated using Ne lines with an uncertainty of $\pm 1 \text{ cm}^{-1}$.

High-pressure diffraction experiments have been performed at ID09A synchrotron beamline (ESRF) using monochromatic x-ray beam ($E = 30$ keV, $\lambda = 0.413$ Å) focused to $15 \times 10 \mu\text{m}^2$ on the sample³⁷. We used a membrane-driven high-pressure cell equipped with Boehler-Almax seats and diamond anvil design, allowing an opening cone of 64° . The culet size was $600 \mu\text{m}$ and the sample was loaded together with He as pressure transmission medium into a hole in a stainless steel gasket preindented to about $80 \mu\text{m}$ with an initial diameter of $300 \mu\text{m}$. Low temperature data were collected in a He-flow cryostat. Single-crystal data have been collected by a vertical-acting ω -axis rotation, with an integrated step scan of 0.5° and a counting time of 1s per frame. Diffraction intensities have been recorded with a Mar555 flat-panel detector. Diffraction data have been processed and analyzed with CrysAlisPro-171.37.35 and Jana2006 software. Pressures were measured with the ruby fluorescence method³⁶.

Density functional theory calculations

Density-functional theory (DFT) calculations were performed using the Vienna Ab-initio Simulation Package (VASP) with projected augmented wave (PAW) potential^{38,39}. The exchange and correlation energy was considered at the generalized gradient approximation (GGA) level for the geometry optimization⁴⁰, and the electronic structure was calculated using the hybrid functional (HSE06)⁴¹. Spin-orbital coupling

was included in all calculations. Van der Waals corrections were included via a pair-wise force field of the Grimme method⁴². In the lattice relaxation, the volumes were fixed while lattice constants and atomic positions were optimized. The pressure was derived by fitting the total energy dependence on the volume with the Murnaghan equation⁴³. After checking the k convergence, the $24 \times 12 \times 8$ and $7 \times 5 \times 3$ k -meshes with Gaussian-type smearing were used for the GGA (Supplementary Fig. 10) and HSE06 calculations, respectively. The band structures, density of states and Fermi surfaces were interpolated in a dense k -mesh of $200 \times 200 \times 200$ using the maximally localized Wannier functions⁴⁴ extracted from HSE06 calculations.

Acknowledgments

Y. Qi acknowledges financial support from the Alexander von Humboldt Foundation. We would like to thank C. Klausnitzer & M. Nicklas for their help with high-pressure magnetic measurements. This work was financially supported by the Deutsche Forschungsgemeinschaft (DFG, Project No. EB 518/1-1 of DFG-SPP 1666 "Topological Insulators") and by a European Research Council (ERC) Advanced Grant, No. (291472) "Idea Heusler".

Author Contributions.

M. A., C. R. and V. S. prepared the samples and performed XRD structural characterization, E. P., P. W. and R. H. performed TEM studies, W. S. performed ambient pressure transport measurements and Meißner effect measurements at low pressures, C. S., T. F. and E. K. performed magneto-transport measurements, Y. Q., P. N., O. B., and S. M. performed high pressure electrical resistivity, Raman spectroscopy and magnetic susceptibility measurements, M. H. performed high pressure single crystal XRD studies, S. W., Y. S. and B. Y. carried out the theoretical calculations. All authors discussed the results of the studies. Y. Q., B. Y., W. S. and S. M. co-wrote the paper. All authors commented on the manuscript.

Competing financial interests.

The authors declare no competing financial interests.

References

1. Wilson, J. A. & Yoffe, A. D. The Transition Metal Dichalcogenides Discussion and interpretation of the observed optical, electrical and structural properties. *Adv. Phys.* **18**, 193-335 (1969).
2. Klemm, R. A. Pristine and intercalated transition metal dichalcogenide superconductors. *Physica C* **514**, 86–94 (2015).
3. Morris, R. C., Coleman, R. V. & Bhandari, R. Superconductivity and magnetoresistance in NbSe₂. *Phys. Rev. B* **5**, 895–901 (1972).
4. Morosan, E. *et al.* Superconductivity in Cu_xTiSe₂. *Nature Phys.* **2**, 544-550 (2006).
5. Moncton, D. E., Axe, J. D. & DiSalvo, F. J. Neutron scattering study of the charge-density wave transitions in 2H-TaSe₂ and 2H-NbSe₂. *Phys. Rev. B* **16**, 801–819 (1977).
6. Qian, X., Liu, J., Fu, L. & Li, J. Quantum spin Hall effect in two-dimensional transition metal dichalcogenides. *Science* **346**, 1344-1347 (2014).
7. Xu, X., Yao, W., Xiao D. & Heinz T. F. Spin and pseudospins in layered transition metal dichalcogenides. *Nature Phys.* **10**, 343–350 (2014).
8. Bates, J. B., Gruzalski, G. R., Dudney, N. J., Luck, C. F. & Yu, X. Rechargeable thin-film lithium batteries. *Solid State Ionics* **70/71**, 619–628 (1994).

9. Li, Y., Wang, H., Xie, L., Liang, Y., Hong, G. & Dai, H. MoS₂ nanoparticles grown on graphene: an advanced catalyst for the hydrogen evolution reaction. *J. Am. Chem. Soc.* **133**, 7296–7299 (2011).
10. Zhang, Y. J., Oka, T., Suzuki, R., Ye, J. T. & Iwasa, Y. Electrically switchable chiral light-emitting transistor. *Science* **344**, 725-728 (2014).
11. Lin, Y.-C., Dumcenco, D. O., Huang, Y.-S. & Suenaga, K. Atomic mechanism of the semiconducting-to-metallic phase transition in single-layered MoS₂. *Nature Nanotech.* **9**, 391-396 (2014).
12. Clarke, R., Marseglia, E. & Hughes, H. P. A low-temperature structural phase transition in β -MoTe₂. *Philos. Mag. B* **38**, 121-126 (1978).
13. Puotinen, D. & Newnhan, R. E. The crystal structure of MoTe₂. *Acta Crystallogr.* **14**, 691-692 (1961).
14. Zandt, T., Dwelk, H., Janowitz, C. & Manzke, R. Quadratic temperature dependence up to 50 K of the resistivity of metallic MoTe₂. *J. Alloy. Compd.* **442**, 216-218 (2007).
15. Brown, B. E. The crystal structures of WTe₂ and high-temperature MoTe₂. *Acta Crystallogr.* **20**, 268–274 (1966).
16. Ali, M. N. *et al.* Large, non-saturating magnetoresistance in WTe₂. *Nature* **514**,

205-208 (2014).

17. Ali, M. N. *et al.* Correlation of crystal quality and extreme magnetoresistance of WTe_2 . *Europhys. Lett.* **110**, 67002 (2015).
18. Pan, X.-C. *et al.* Pressure-driven dome-shaped superconductivity and electronic structural evolution in tungsten ditelluride. *Nature Commun.* **6**, 7805 (2015).
19. Kang, D. *et al.* Superconductivity emerging from suppressed large magnetoresistant state in WTe_2 . *Nature Commun.* **6**, 7804 (2015).
20. Zhu, Z. *et al.* Quantum Oscillations, Thermoelectric Coefficients, and the Fermi Surface of Semimetallic WTe_2 . *Phys. Rev. Lett.* **114**, 176601 (2015).
21. Soluyanov, A. *et al.* Type II Weyl Semimetals. Preprint at <http://arxiv.org/abs/1507.01603> (2015).
22. Rifliková, M., Martoňák, R. & Tosatti, E. Pressure-induced gap closing and metallization of MoSe_2 and MoTe_2 . *Phys. Rev. B* **90**, 035108 (2014).
23. Fu, L. & Kane, C. L. Superconducting Proximity Effect and Majorana Fermions at the Surface of a Topological Insulator. *Phys. Rev. Lett.* **100**, 096407 (2008).
24. Sun, Y., Wu, S.-C., Ali, M. N., Felser, C. & Yan, B. Prediction of the Weyl semimetal in the orthorhombic MoTe_2 . *Phys. Rev. B* **92**, 161107 (2015).
25. Cho, G. Y., Bardarson, J. H., Y.-M. Lu, & Moore, J. E. Superconductivity of doped

- Weyl semimetals: Finite-momentum pairing and electronic analog of the $^3\text{He-A}$ phase. *Phys. Rev. B* **86**, 214514 (2012).
26. Wei, H., Chao, S.-P. & Aji, V. Odd-parity superconductivity in Weyl semimetals. *Phys. Rev. B* **89**, 014506 (2014).
27. Hosur, P., Dai, X., Fang, Z. & Qi, X.-L. Time-reversal-invariant topological superconductivity in doped Weyl semimetals. *Phys. Rev. B* **90**, 045130 (2014).
28. Jian, S.-K., Jiang, Y.-F. & Yao, H. Emergent Spacetime Supersymmetry in 3D Weyl Semimetals and 2D Dirac Semimetals. *Phys. Rev. Lett.* **114**, 237001 (2015).
29. Keum, D. H. *et al.* Bandgap opening in few-layered monoclinic MoTe_2 . *Nature Phys.* **11**, 482–487 (2015).
30. Hughes, H. P. & Friend, R. H. Electrical resistivity anomaly in $\beta\text{-MoTe}_2$. *J. Phys. C: Solid State Phys.* **11**, L103-L105 (1978).
31. Hulliger, F. Crystal Chemistry of the Chalcogenides and Pnictides of the Transition Elements, in *Structure and Bonding* 83-229, (Structure and Bonding vol. 4, Springer-Verlag, New York, Heidelberg, Berlin 1968).
32. Suderow, H., Tissen, V. G., Brison, J. P., Martínez, J. L. & Vieira, S. Pressure induced effects on the Fermi surface of superconducting 2H-NbSe_2 . *Phys. Rev. Lett.* **95**, 117006 (2005).

33. Müller, K. H., Fuchs, G., Handstein, A., Nenkov, K., Narozhnyi, V.N., & Eckert, D. The upper critical field in superconducting MgB₂. *J. Alloy. Compd.* **322**, L10-L13 (2001).
34. Wang, Z. *et al.* MoTe₂: Weyl and Line Node Topological Metal. Preprint at <http://arxiv.org/abs/1511.07440> (2015).
35. Fourcaudot, G., Gourmala, M., & Mercier, J. Vapor phase transport and crystal growth of molybdenum trioxide and molybdenum ditelluride. *J. Cryst. Growth* **46**, 132-135 (1979).
36. Mao, H. K., Xu, J., & Bell, P. M. Calibration of the ruby pressure gauge to 800 kbar under quasi-hydrostatic conditions. *J. Geophys. Res.* **91**, 4673-4676 (1986).
37. Merlini, M. & Hanfland, M. Single-crystal diffraction at megabar conditions by synchrotron radiation. *High Pressure Res.* **33**, 511-522 (2013).
38. Kresse, G. & Hafner, J. *Ab initio* molecular dynamics for open-shell transition metals. *Phys. Rev. B* **48**, 13115-13118 (1993).
39. Kresse, G. & Furthmüller, J. Efficiency of ab-initio total energy calculations for metals and semiconductors using a plane-wave basis set. *Comp. Mater. Sci.* **6**, 15-50 (1996).
40. Perdew, J. P., Burke, K., & Ernzerhof, M. Generalized Gradient Approximation

- Made Simple. *Phys. Rev. Lett.* **77**, 3865-3868 (1996).
41. Heyd, J., Scuseria, G. E. & Ernzerhof, M. Hybrid functionals based on a screened Coulomb potential. *J. Chem. Phys.* **118**, 8207-8215 (2003).
42. Grimme, S. Semiempirical GGA-Type Density Functional Constructed with a Long-Range Dispersion Correction. *J. Comput. Chem.* **27**, 1787-1799 (2006).
43. Murnaghan, F. D. The Compressibility of Media under Extreme Pressures. *P. Natl. Acad. Sci. U.S.A.* **30**, 244-247 (1944).
44. Marzari, N. & Vanderbilt, D. Maximally localized generalized Wannier functions for composite energy bands. *Phys. Rev. B* **56**, 12847-12865 (1997).

Figure Captions

Figure 1. MoTe₂ crystal structure. (a) HAADF-STEM image of 1T'-MoTe₂ along the [100] zone (scale bar, 0.5 nm). The red rectangle shows HAADF simulated image, and the red and blue spheres in the yellow rectangle represent Te and Mo atoms, respectively. (b) Corresponding electron diffraction images. (c) 1T' and T_d-MoTe₂ crystal structures. (d) Energy-volume dependence for 1T' and T_d phases from DFT calculations.

Figure 2. Resistivity of 1T'-MoTe₂ at ambient pressure. (a) Temperature-dependent resistivity at near zero pressure. Inset: Anomaly with hysteresis observed at approximately 250 K. This hysteresis is associated with the structural phase transition from 1T'-MoTe₂ to T_d-MoTe₂. (b) Resistivity detail from 0.08–1.2 K. Superconductivity is observed with onset at ≈ 0.3 K and zero resistance at $T_c = 0.10$ K.

Figure 3. Transport properties of 1T'-MoTe₂ as a function of pressure. (a) Electrical resistivity as a function of temperature for pressures of 0.76–34.9 GPa. The anomaly associated with the structural transition is completely suppressed with increasing pressure. (b), (c) Electrical resistivity as a function of temperature for pressures of 0.7–11.7 and 11.7–34.9 GPa, respectively. Clear electrical resistivity drops

and zero-resistance behavior are apparent. T_c increases under increasing pressure and a dome-shaped superconducting phase in pressure-temperature space is observed for the maximum superconducting transition temperature corresponding to $T_c = 8.2$ K at 11.7 GPa. **(d)** Temperature dependence of resistivity under different magnetic fields of up to 3 T at 11.2 GPa. **(e)** Temperature dependence of MoTe₂ upper critical field H_{c2} determined using 90% points on resistivity transition curves. The red curve is the best-fit line.

Figure 4. High pressure Raman spectroscopy and structural studies of 1T'-MoTe₂.

(a), Pressure-dependent Raman signals for 1T'-MoTe₂ at room temperature. The Raman spectra contain two characteristic peaks due to the A_g and B_g vibrational modes of the 1T'-MoTe₂ structure. **(b)** Frequencies of A_g and B_g modes as function of pressure. The frequencies of both vibrational modes increase gradually and continuously as the pressure increases. **(c)** Pressure dependence of the monoclinic angle β obtained from single crystal x-ray diffraction studies. Isothermal compression at room temperature (red circles) shows increase of the monoclinic distortion with pressure whereas reversible orthorhombic T_d – monoclinic 1T' transition is observed in isothermal compression (filled blue circles) / decompression (open blue circles) run at 135 K. The error bars in (b) and (c) due to s. d. are smaller than the symbols size.

Figure 5. MoTe₂ electronic phase diagram. The black and green square represents the structural phase transition temperature T_s obtained from resistivity and single crystal synchrotron x-ray diffraction data. The red, blue, and olive circles represent the T_c extracted from various electrical resistance measurements, and the pink triangles represent the T_c determined from the magnetization measurements. The error bars in due to s. d. are smaller than the symbols size.

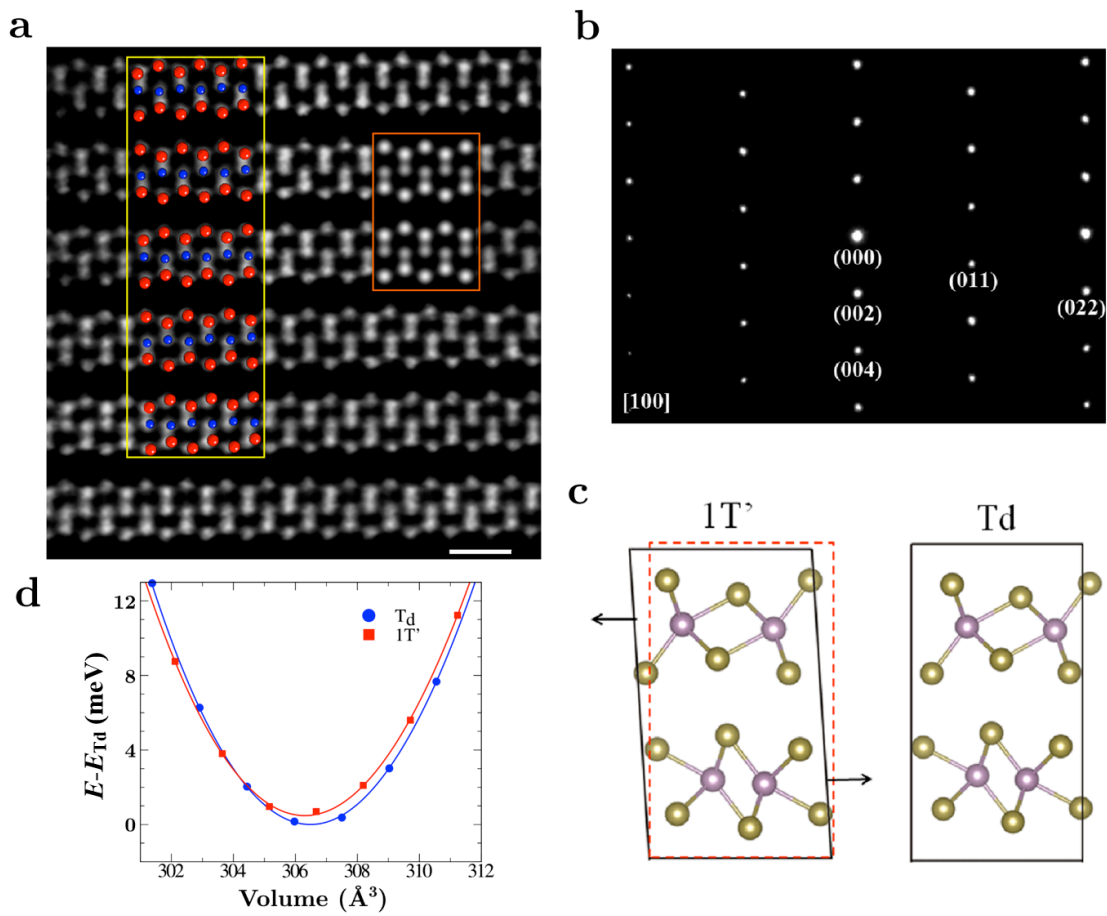


Fig. 1 Qi et al

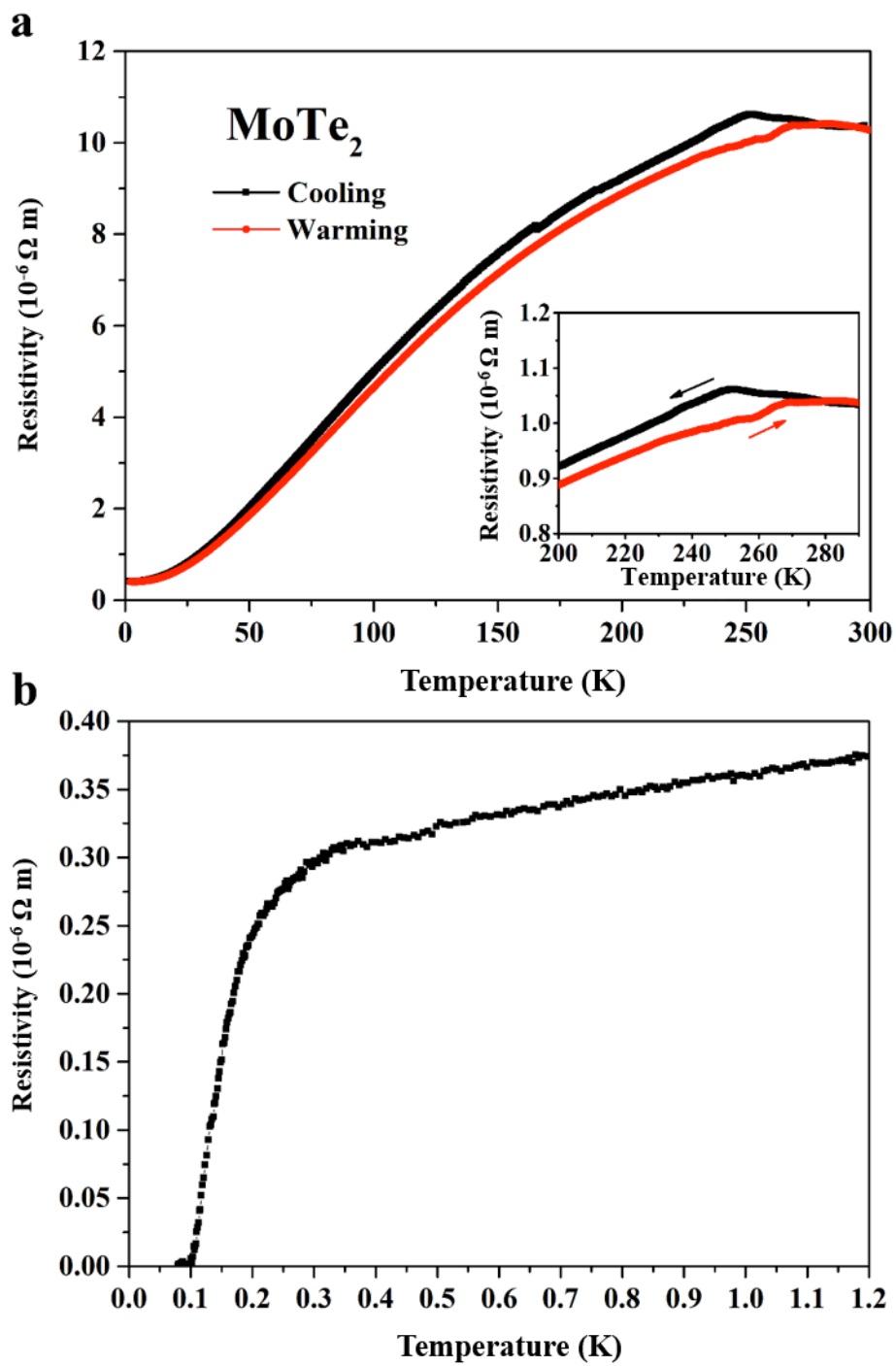


Fig. 2 Qi et al.

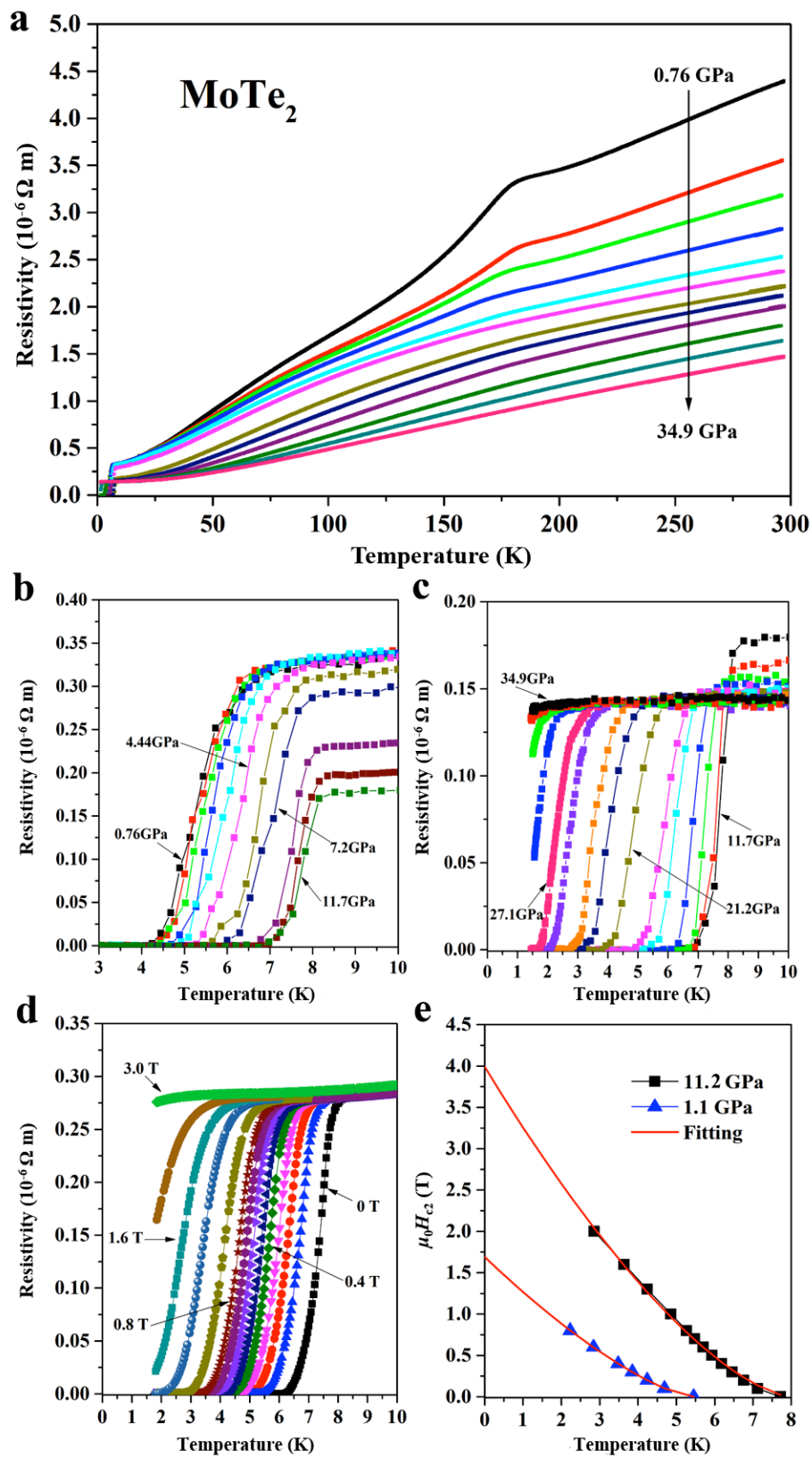


Fig. 3 Qi et al.

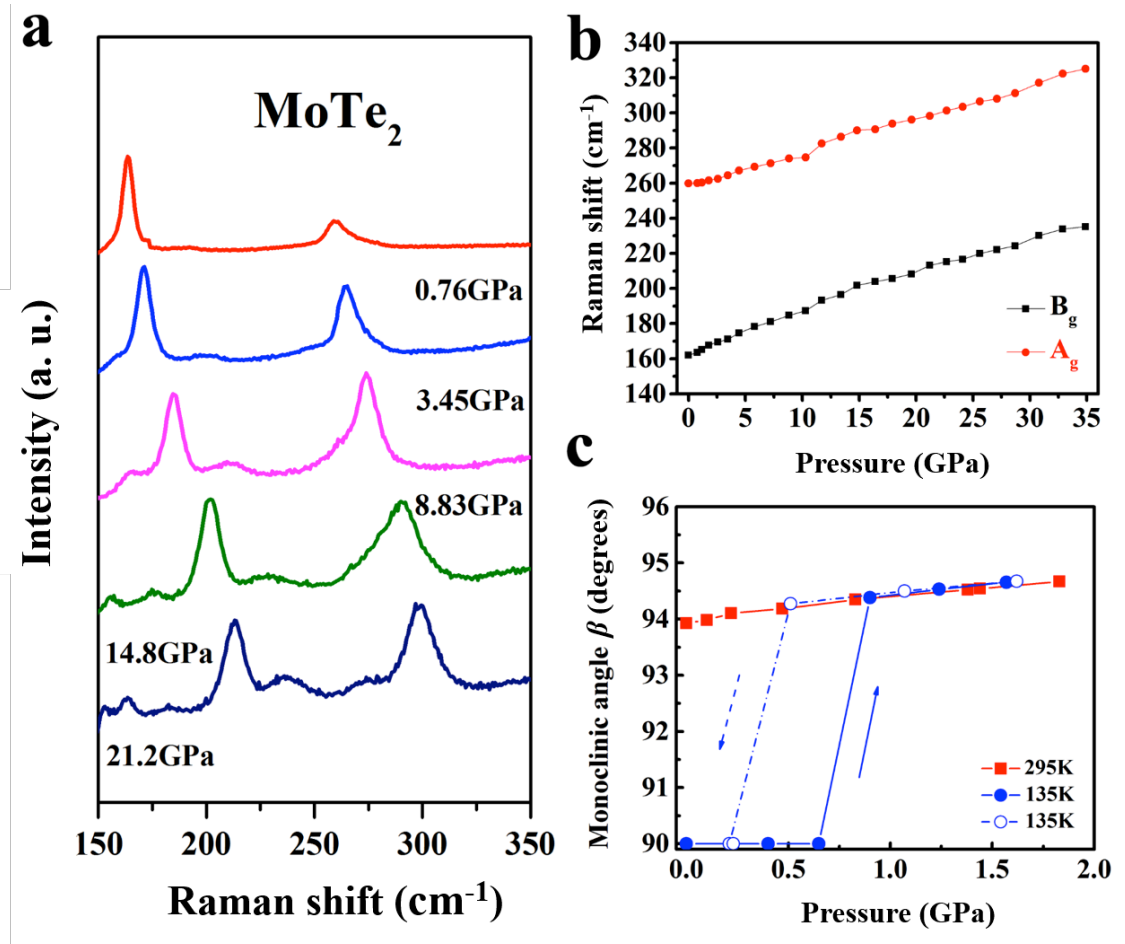


Fig. 4 Qi et al

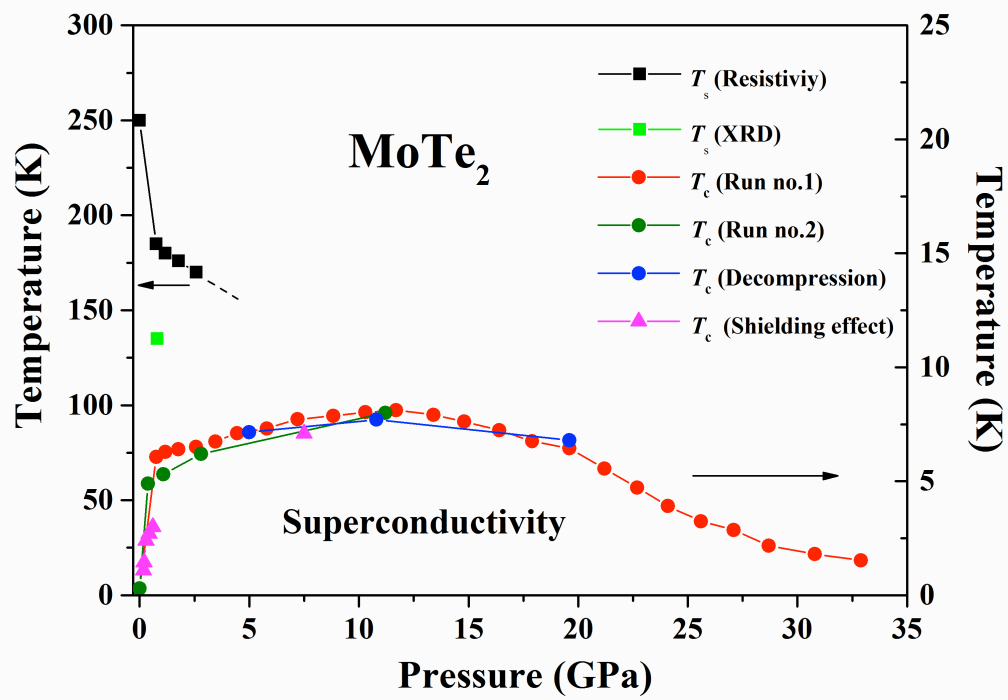
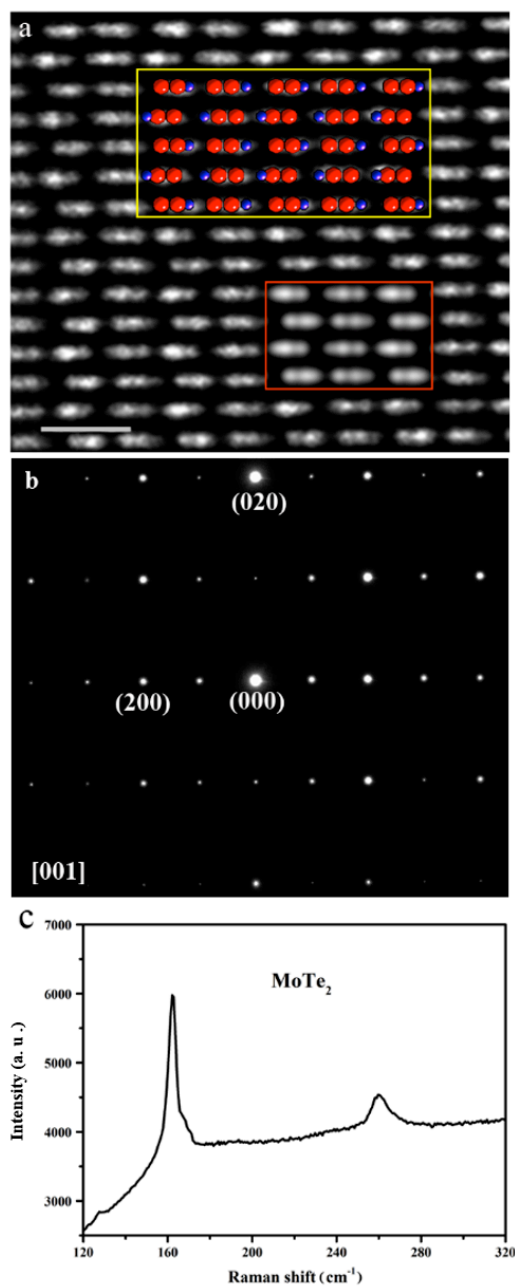
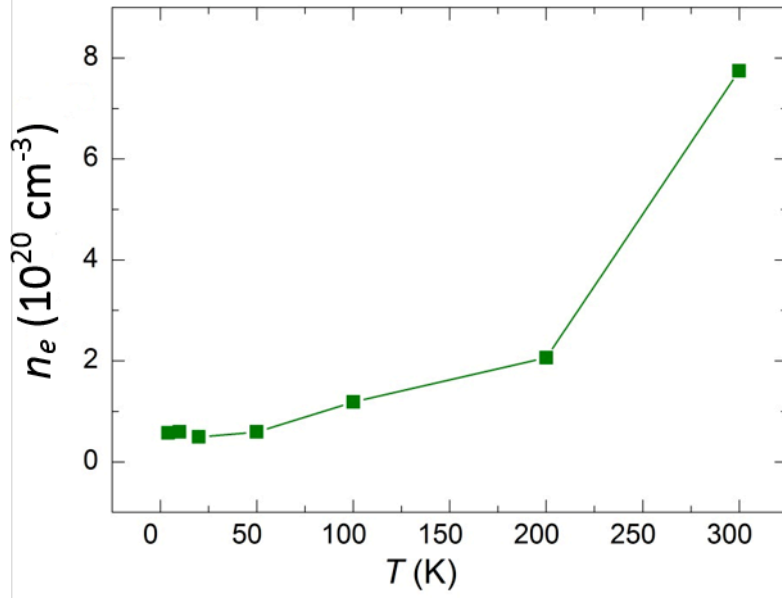


Fig. 5 Qi et al.

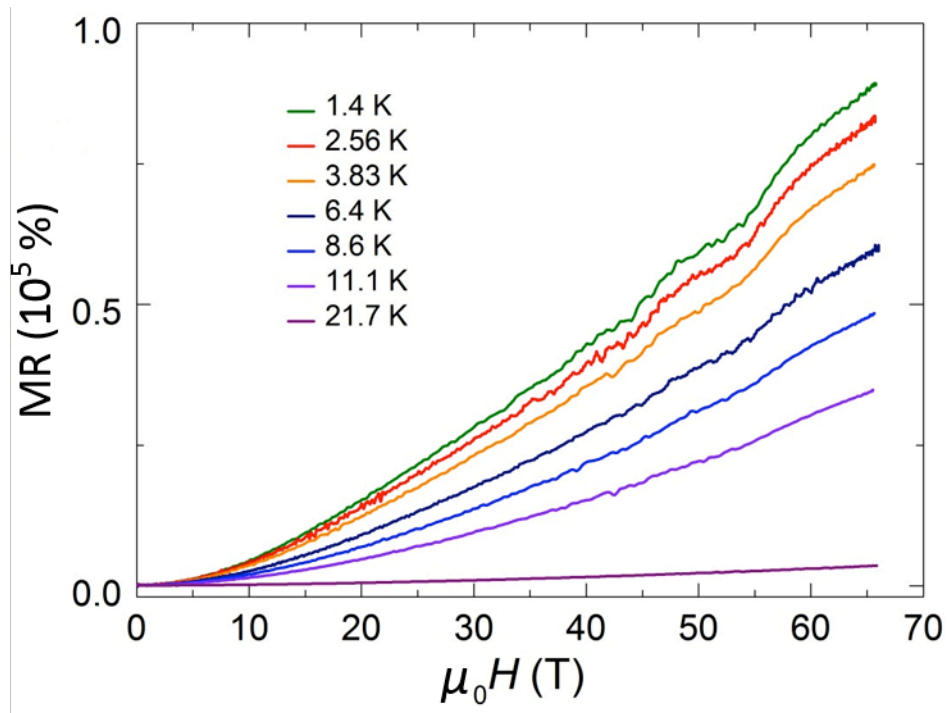
Supplementary Figures



Supplementary Figure 1. Crystal structure of 1T'-MoTe₂. (a) HAADF-STEM image of 1T'-MoTe₂, looking down the [001] zone (scale bar, 0.5 nm). The area indicated by the red rectangle shows HAADF simulated image. The red spheres represent Te atoms and blue spheres represent Mo atoms. (b) The corresponding electron diffraction image. (c) Raman signals for 1T'-MoTe₂ at ambient pressure.

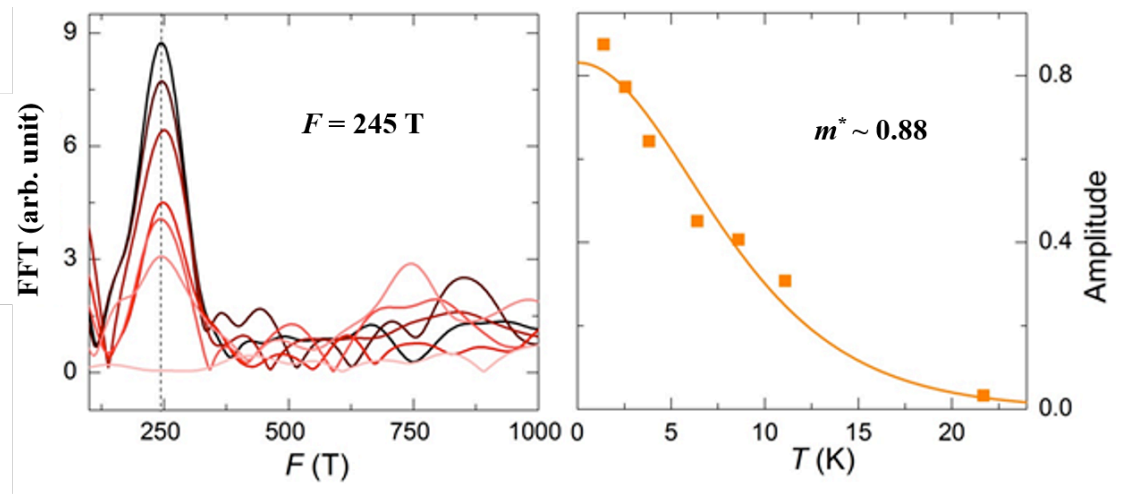


Supplementary Figure 2. Electron charge carrier density of 1T'-MoTe₂.

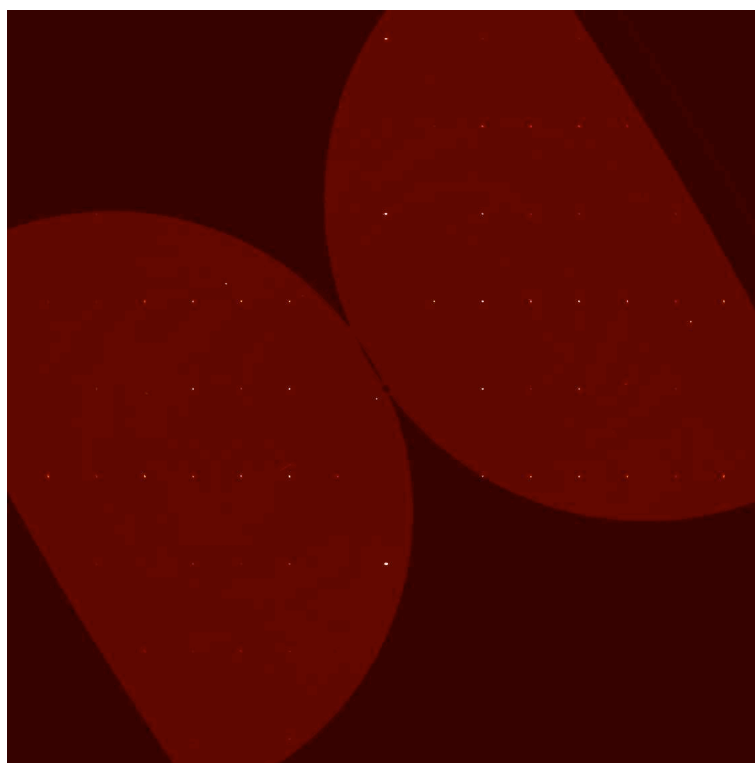


Supplementary Figure 3. Magnetoresistance measured up to a field $\mu_0 H = 66$ T.

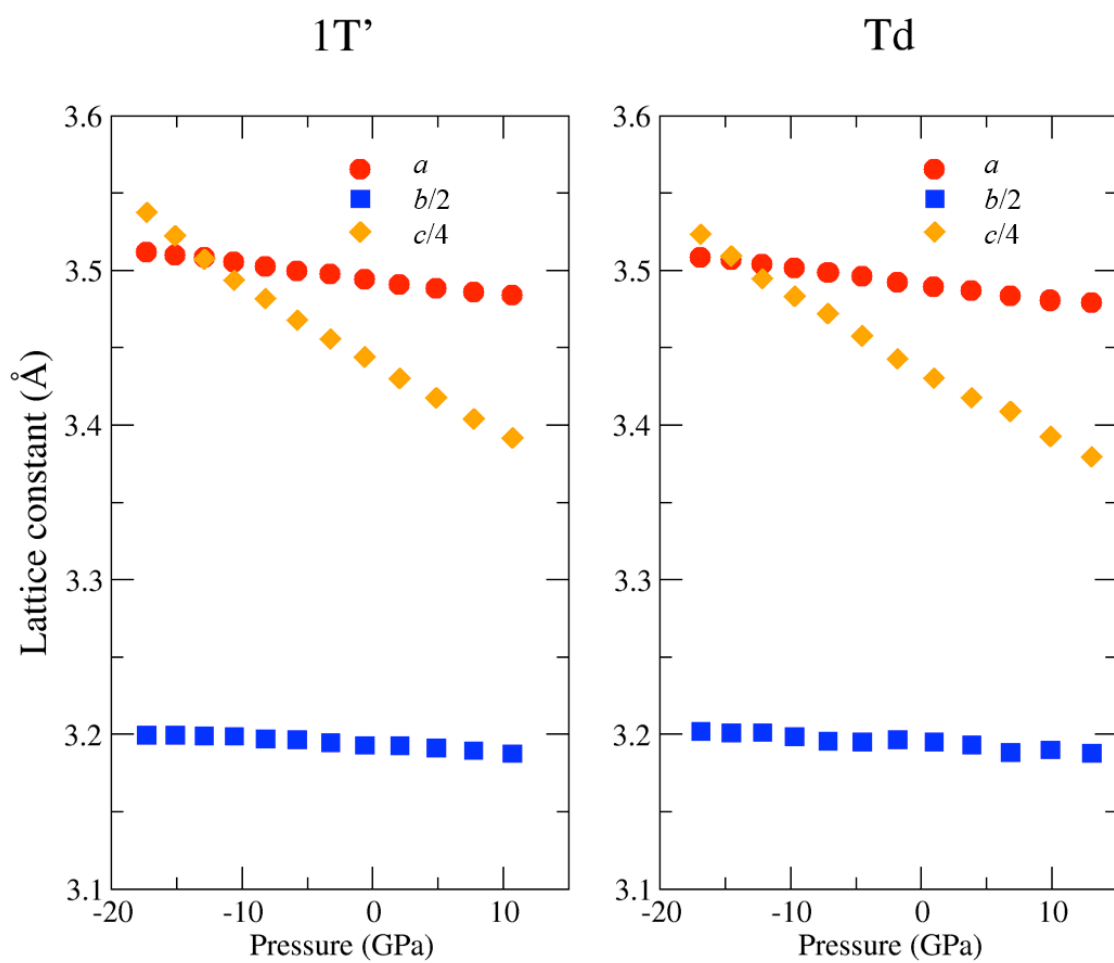
Magneto-resistivity superimposed with quantum oscillations known as Shubnikov-de Haas (SdH) oscillations.



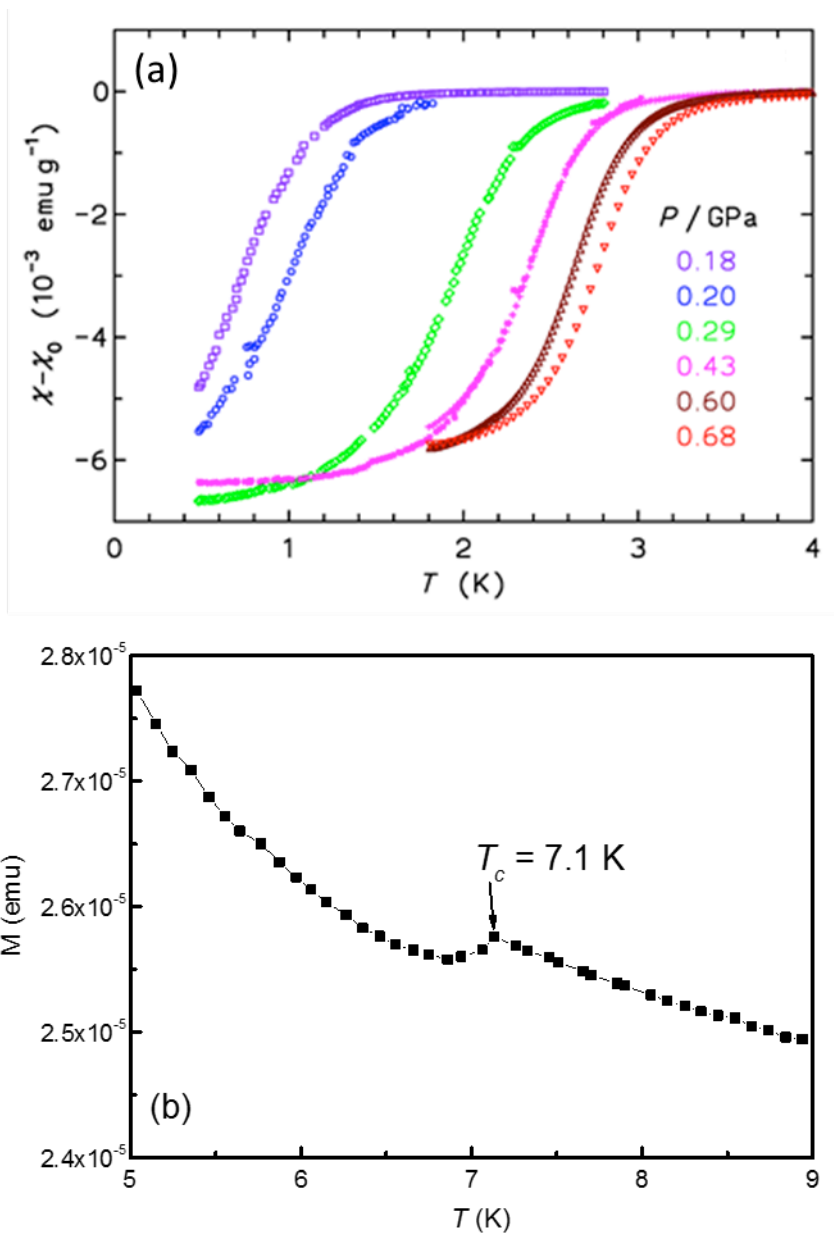
Supplementary Figure 4. Fast Fourier transformation of SdH oscillations. (a) The fast Fourier transformation (FFT) of the SdH oscillations. **(b)** Temperature dependent SdH oscillations amplitude.



Supplementary Figure 5. Reciprocal space reconstruction of the $hk0$ plane based on single-crystal diffraction data of β -MoTe₂ collected at pressure 1.56 GPa and temperature 120 K.

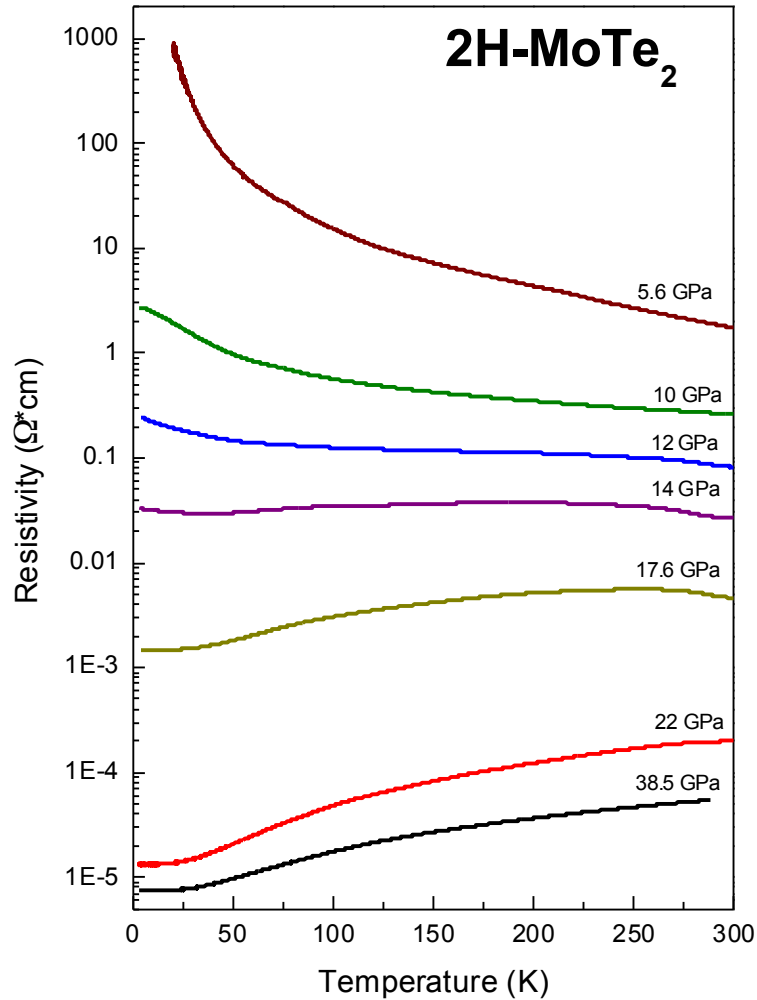


Supplementary Figure 6. Lattice parameters as a function of pressure for T_d and 1T' phases from GGA calculations.

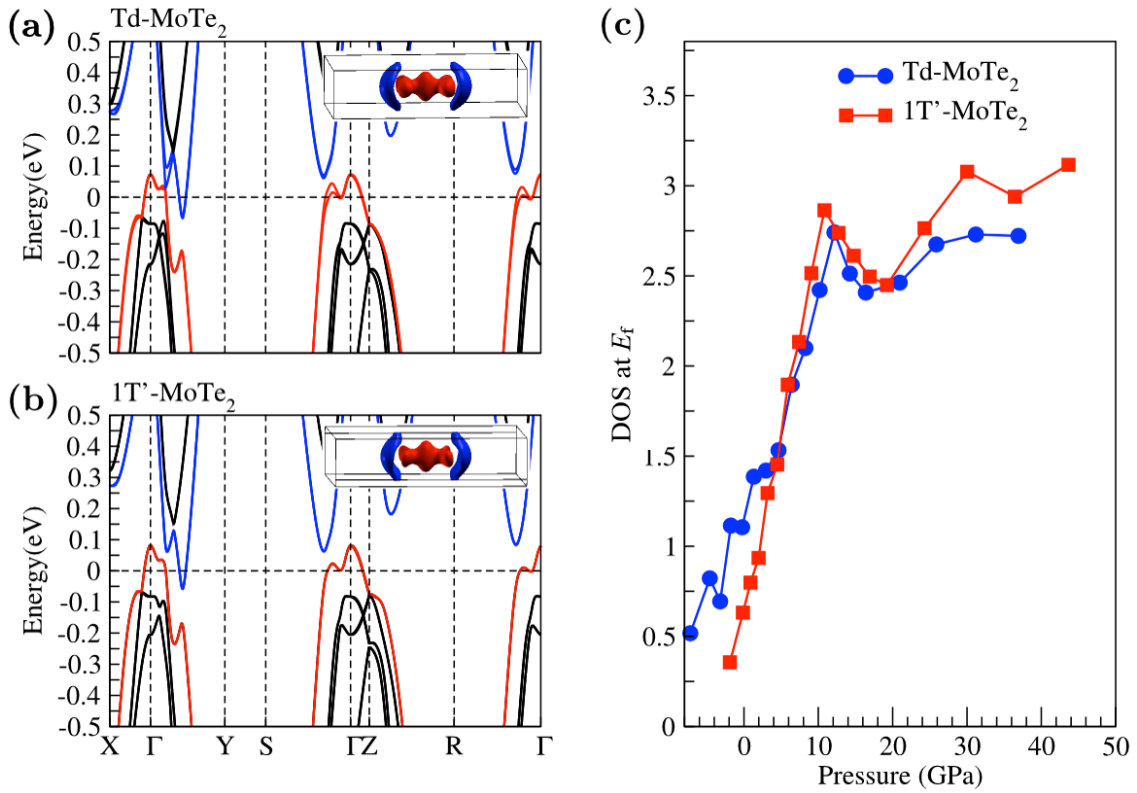


Supplementary Figure 7. Magnetic shielding effect measurements at high pressure.

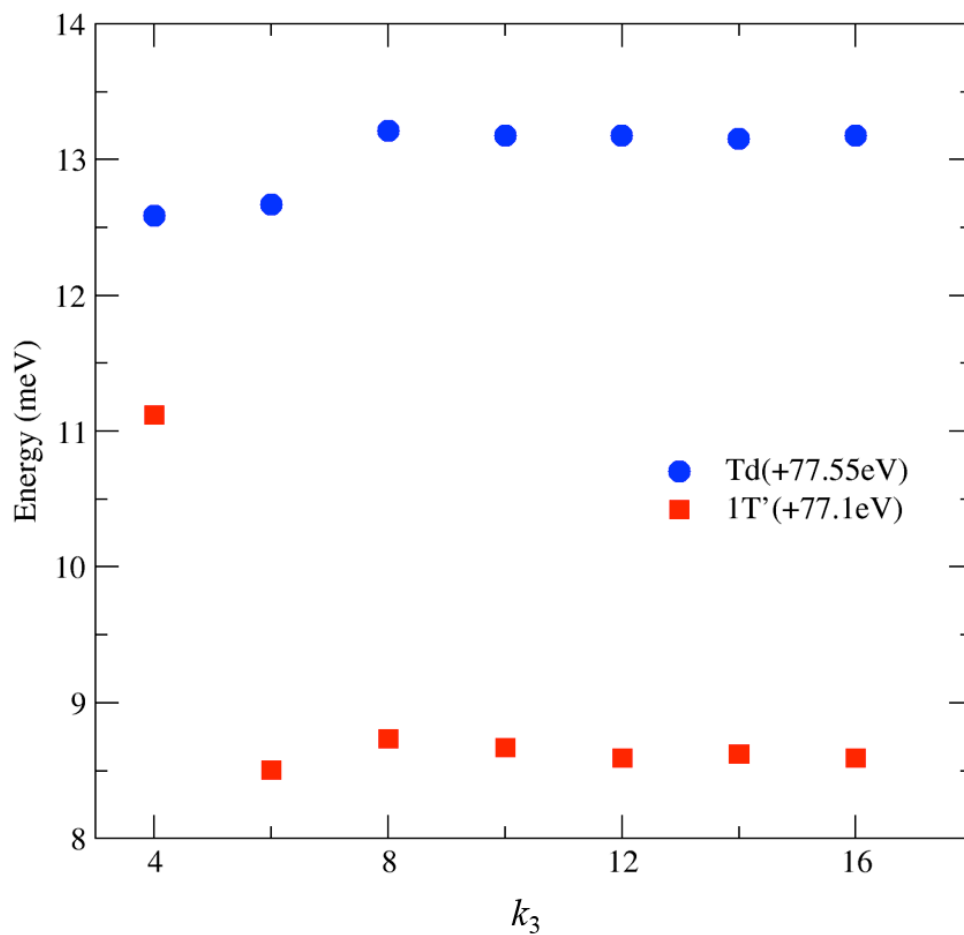
(a) The magnetic susceptibility for $P < 0.7$ GPa, (b) The raw magnetization signal at $P = 7.5$ GPa for MoTe_2 , both as a function of temperature in a miniature high-pressure cell¹.



Supplementary Figure 8. Temperature dependence of the resistivity of 2H-MoTe₂ under high pressure up to nearly 40 GPa. At pressures below 15 GPa, 2H-MoTe₂ remains semiconducting. By 16 GPa, 2H-MoTe₂ shows metallic-like behavior the whole temperature range. Thus, 2H-MoTe₂ undergoes an insulator-to-metal transition at around 16 GPa, in good agreement with recent theoretical predictions. No signs of superconductivity ($T_c > 1.5$ K) have been found up to nearly 40 GPa.



Supplementary Figure 9. Electronic structures obtained from DFT calculations. (a) and **(b)** Electronic band structures and Fermi surfaces for MoTe₂ in T_d and 1T'-MoTe₂ phases respectively with experimental lattice constants. Red and blue Fermi surfaces are hole and electron pockets, respectively. **(c)** The evolution of the density of states (DOS) at the Fermi level as a function of pressure. Please note that a different setting of the elementary cell was used in a previous report².



Supplementary Figure 10. k grid convergence in DFT (GGA) calculations. We use k_3 to represent the k -point density in reciprocal space. The k points in three directions have the relation of $3k_1=3k_2/2=k_3$. The convergence arrives at $k_3=8$.

Supplementary Tables

Phase	T _d -MoTe ₂ (γ -MoTe ₂)
Symmetry	Orthorhombic, <i>Pmn</i> 2 ₁ (No. 31)
Cell Parameters (Å)	$a = 3.477(2)$, $b = 6.335(3)$, $c = 13.889(6)$ $\alpha = \beta = \gamma = 90^\circ$
Wavelength (Å)	Mo <i>K</i> α - 0.71073
V (Å ³)	305.97(20)
Z	4
Calculated Density (g cm ⁻³)	7.622(6)
Formula Weight (g mol ⁻¹)	351.14
Absorption Coefficient (mm ⁻¹)	22.64
F_{000}	584.0
Reflections	3328
Data/Restraints/Parameters	832 / 38 / 1
Difference e-density (e/ Å ³)	+2.74 to -1.76
R_1 (all reflections)	0.0359
R_1 $F_o > 2\sigma(F_o)$	0.0312
wR_2 (all)	0.076
$R_{int}/R(\sigma)$	0.0812/0.0192
Goof	1.044

Supplementary Table 1. Single crystal structure determination for T_d-MoTe₂ (γ -MoTe₂), experimental data taken at 120 K.

T _d -MoTe ₂					
Atom	Wyckoff Site	<i>x</i>	<i>y</i>	<i>z</i>	Occupation
Mo1	2 <i>a</i>	0	0.6052(2)	0.5003(1)	1
Mo2	2 <i>a</i>	0	0.0301(2)	0.0147(1)	1
Te1	2 <i>a</i>	0	0.8626(2)	0.6557(1)	1
Te2	2 <i>a</i>	0	0.6405(2)	0.1125(1)	1
Te3	2 <i>a</i>	0	0.2900(2)	0.8593(1)	1
Te4	2 <i>a</i>	0	0.2160(2)	0.4027(1)	1

Supplementary Table 2. Refined structural parameters for T_d-MoTe₂ at 120 K.

	Unit cell Volume (\AA^3)		Lattice parameters (\AA)							
	Exp.	The.	<i>a</i>		<i>b</i>		<i>c</i>		<i>β</i>	
			Exp.	The.	Exp.	The.	Exp.	The.	Exp.	The.
T _d	305.97	306.30	3.477	3.506	6.335	6.360	13.889	13.746	90	90
1T'	303.64	306.48	3.469	3.495	6.330	6.392	13.860	13.741	93.917	93.8576

Supplementary Table 3. Lattice parameters from experimental measurements (Exp.) and DFT relaxation (The.).

Supplementary Note 1

We measured temperature dependent four-probe Hall resistivity in a field-sweep, $\rho_{xy}(H)$ to derive the Hall coefficient, $R_H(T)$, and type of carrier, where Hall coefficient directly gives the carrier concentration of a material. Importantly, $\rho_{xy}(H)$ exhibits a linear characteristic up to fields of 9 T. 1T'-MoTe₂ exhibits negative Hall coefficient, reflecting electrons as a major charge carriers in the whole temperature range. To calculate the electron charge density, n_e , we used the Drude single-band model³, $n_e(T) = 1/[e R_H(T)]$, where e is the elementary charge. The estimated values of n_e are $5 \times 10^{19} \text{ cm}^{-3}$ at 2 K and $8 \times 10^{20} \text{ cm}^{-3}$ at 300 K (Supplementary Fig. 2), close to those reported⁴.

Magnetoresistance (MR) is defined as the ratio of the change in resistivity due to the applied magnetic field, $\text{MR} = \rho_{xy}(H)/\rho_{xy}(0) - 1$. Here, we measured transverse MR (Supplementary Fig. 3). Resistivity of T_d-MoTe₂ is very sensitive to applied field and shows MR of 10⁵ % at 1.4 K without any sign of saturation up to $\mu_0 H = 66$ T. More interestingly, these MR data display Shubnikov-de Haas (SdH) oscillations.

To calculate the amplitude of the SdH oscillations, we fit a 3rd order polynomial to the field dependent resistivity at each temperature. Supplementary Fig. 4a shows the fast Fourier transformation (FFT) of the SdH oscillations that exhibits a cyclotron frequency of the electrons at 245 T. This frequency is equivalent to the periodicity $1/B \approx 0.004 \text{ T}^{-1}$ that corresponds to a cross-sectional area of the Fermi surface $A_F = 0.024 \text{ \AA}^{-2}$ from the Onsager relationship $F = \Phi_0 / (2\pi^2) A_F$, where Φ_0 is the magnetic flux quantum. A very small Fermi momentum $k_F = 0.087 \text{ \AA}^{-1}$ is obtained supposing a circular cross-section. Further, the cyclotron effective mass of the carriers is determined by fitting the following Lifshitz-Kosevich temperature reduction term⁵ to the temperature

dependent SdH oscillations amplitude (Supplementary Fig. 4b).

$$\frac{\Delta\rho_{xx}}{\rho_{xx}}(T) = \frac{14.69m^*T/B}{\sinh(14.69m^*T/B)}$$

The obtained effective mass, m^* is $0.88 m_0$, where m_0 is the bare mass of the electron. A lower m^* is observed in few-layer 1T'-MoTe₂ specimens³.

Supplementary Note 2

Consistent with previous reports⁶, our calculations show that both T_d-MoTe₂ and 1T'-MoTe₂ are semimetals at zero pressure, as presented in Supplementary Fig. 9. Since the lattices for two phases are very close, their electronic structures are very similar to each other. As layered compounds, band dispersion is strong in the X-Γ-Y plane and weak along the Γ-Z direction. In the inset of Supplementary Fig. 9a and b, the Fermi surfaces are shown with hole and electron pockets located around the Γ point and the middle of Γ-Y, respectively. One main difference between them is the spin degeneracy. Due to the lack of inversion symmetry, band splitting occurs for spin-up and spin-down states in T_d-MoTe₂. In contrast, the 1T' phase has inversion symmetry and all the bands are spin degenerated. At the charge neutral point, we calculated the extreme Fermi surface area of the electron and hole pockets for both two phases. The electron pockets for T_d phase are 0.021 and 0.019 Å⁻², which correspond to quantum oscillation frequencies of 221 and 200 T, respectively, according to the Onsager relation. Closely, the electron pocket in 1T' phase is 0.0169 Å⁻², corresponding to a quantum oscillation frequency of 178 T. The extreme Fermi surface area of hole pockets are much larger than 700 T. So we attribute the experimentally observed SdH oscillations frequency (Supplementary Fig. 4) to the electron pockets. The smaller theoretical frequency value, compared with experiment, may indicate that the sample is slightly electron-doped. Since the electron

pocket areas are very close in the two phases, the measured quantum oscillations cannot distinguish them.

In Supplementary Fig. 6 the evolution of the lattice and electronic structures under pressure is shown. Due to van der Waals interactions, the lattice parameter c is compressed strongly by the applied pressure, while a and b only reduce slightly. When the compressive pressure increases from zero to 20 GPa, the density of states (DOS) at the Fermi energy first increases quickly and then decrease slightly after a maximum at around 10 GPa for both T_d and $1T'$ phases (Supplementary Fig. 9c). This pressure dependence of DOS may be relevant to the dome-shape superconductivity observed in our experiment, since conventional superconductivity is known to be sensitive to the DOS at the Fermi energy.

Supplementary References

1. Alireza, P. L. & Lonzarich, G. G., Miniature anvil cell for high-pressure measurements in a commercial superconducting quantum interference device magnetometer. *Rev. Sci. Instrum.* **80**, 023906 (2009).
2. Sun, Y., Wu, S.-C., Ali, M. N., Felser, C., Yan, B. Prediction of the Weyl semimetal in the orthorhombic MoTe₂. *Phys. Rev. B* **92**, 161107 (2015).
3. Ashcroft, N. W. and Mermin, N. D. *Solid State Physics* (Harcourt, 1976).
4. Keum, D. H. *et al.* Bandgap opening in few-layered monoclinic MoTe₂. *Nature Phys.* **11**, 482–486 (2015).
5. Shoenberg, D. *Magnetic Oscillations in Metals*. Cambridge University Press (2009).
6. Dawson, W. G. & Bullett, D. W. Electronic structure and crystallography of MoTe₂ and WTe₂. *J. Phys. C: Solid State Phys.* **20**, 6159-6174 (1987).